ACS NANO

www.acsnano.org

Multidimensional Imaging Reveals Mechanisms Controlling Multimodal Label-Free Biosensing in Vertical 2DM-Heterostructures

Tetyana Ignatova,[*,⊥] Sajedeh Pourianejad, Xinyi Li, Kirby Schmidt, Frederick Aryeetey, Shyam Aravamudhan, and Slava V. Rotkin[*,⊥]

Cite This: https://doi.org/10.1021/acsnano.1c09335 Read Online

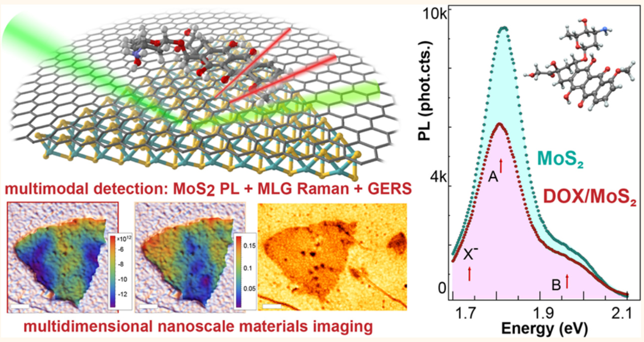

ABSTRACT: Two-dimensional materials and their van der Waals heterostructures enable a large range of applications, including label-free biosensing. Lattice mismatch and work function difference in the heterostructure material result in strain and charge transfer, often varying at a nanometer scale, that influence device performance. In this work, a multidimensional optical imaging technique is developed in order to map subdiffractional distributions for doping and strain and understand the role of those for modulation of the electronic properties of the material. As an example, vertical heterostructures comprised of monolayer graphene and single-layer flakes of transition metal dichalcogenide MoS_2 were fabricated and used for biosensing. Herein, the optical label-free detection of doxorubicin, a common cancer drug, is reported *via* three independent optical detection channels (photoluminescence shift, Raman shift, and graphene enhanced Raman scattering). Non-uniform broadening of components of multimodal signal correlates with the statistical distribution of local optical properties of the heterostructure. Multidimensional nanoscale imaging allows one to reveal the physical origin for such a local response and propose the best strategy for the mitigation of materials variability and future device fabrication, enabling multiplexed biosensing.

KEYWORDS: *materials physics, 2D van der Waals stack heterostructure, multimodal optical characterization, graphene biosensors, transition metal dichalcogenide biosensors*

INTRODUCTION

The emergent need to achieve better, more precise, and sensitive drug detection in medicine and health care has been recently addressed by developing biosensors based on two-dimensional materials (2DM).[1−9] Not only do 2D materials introduce several response and/or transduction mechanisms and offer better performance but also they can be used for label-free biosensing. Importantly, 2DMs could be designed and/or integrated to generate several signals in response to a single analyte, as it will be illustrated below, or to respond by several channels to a group of substances in parallel, thus achieving a multiplexed detection.

The multimodal operation exceeds single-mode biosensing through its higher throughput (it allows detection of several materials properties at once) as well as the ability to differentiate the analyte from background signals in a complex media. It potentially allows the multiplexing of biosensing,[10−14] *i.e.*, determining multiple analytes through a single test.

While significant attention has been paid to exploring a range of 2D materials and demonstrating their biosensing capabilities at the level of single devices,[15−18] overall knowledge on what allows successful multimodal detection and what limits biosensing capabilities of 2DM heterostructures is scarce. Atomically thin 2D materials, having an ultimate surface-to-volume ratio, may possess surface non-

Received: October 21, 2021
Accepted: January 14, 2022

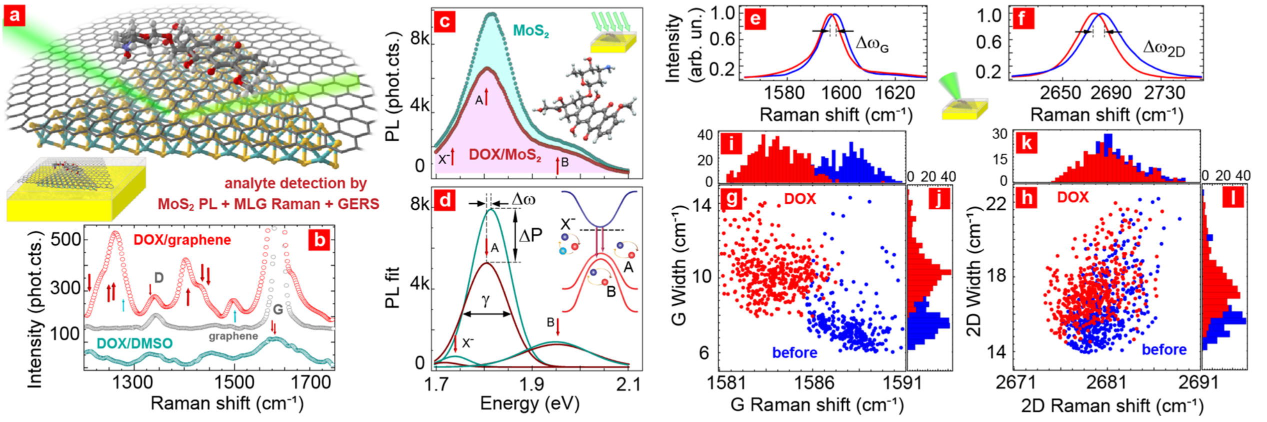

Figure 1. Multiplexed detection of doxorubicin (DOX) drug in 2DM vertical heterostructure by the combination of MoS$_2$ photoluminescence, DOX GERS, and Raman shift of graphene. (a) Schematics of an analyte molecule on monolayer graphene (MLG) surface, above a MoS$_2$ island, supported by Si/SiO$_2$ substrate (shown in inset). (b) GERS signal of DOX/MLG (red), vs reference Raman spectra of DOX/DMSO solution (cyan), and MLG (gray); red (cyan) arrows mark DOX (DMSO) lines. (c) Modulation of MoS$_2$ PL spectrum: with DOX (red) and w/o DOX (cyan); inset shows DOX molecular structure. (d) Fitting of measured PL spectra from (c): A/B-exciton and trion (X$^-$) lines are shown; modulation of peak position (Δ*ω*) and intensity (Δ*P*) are indicated using A-exciton fit; inset shows the schematics of optical subbands of MoS$_2$. (e and f) Typical G and 2D-Raman spectra of MLG: with DOX (red) and before incubation (blue); G and 2D-line intensities were normalized to unity. (g and h) Correlation plots and (i–l) partial distribution functions for peak position and width for G- and 2D-lines, measured locally, at diffraction limited spots across the sample; same color code as in (e and f); clear line red shift and broadening are detected with DOX.

uniformities at the nanometer scale (atomic impurities/adsorbates/defects, wrinkles/ruptures) that modulate their optical properties. Though, the importance and explicit role of these non-uniformities in variability of materials' properties is yet to be understood. To a large extent, the difficulty to determine physical mechanisms that control performance of 2DM devices is due to disparate scales for atomic non-uniformities compared to the size of active elements of a biosensor, which are often a micrometer or larger. Structural characterization with a high spatial resolution, capable to resolve such defects, such as electron microscopy, often does not detect materials optical properties, while optical microscopy lacks the required resolution. Thus, in order to reveal mechanisms that control sensing, multiple characterization tools should be combined and correlated.[19] In this work, correlated multidimensional imaging, including Raman and near-field microscopies, scanning probe, and electron microscopies, was applied to unveil physical processes behind label-free multimodal detection of doxorubicin (DOX), an anthracycline cancer drug, by 2DM vertical heterostructures.

Doxorubicin is one of the most common drugs against different types of cancer (hematological, thyroid, breast, ovarian, lung, and liver cancer).[20−24] Since DOX is known for certain drug resistance and side effects,[25−28] an efficient and sensitive detection of the amount of DOX in various types of biological samples, potentially at the point-of-care, has a significant value. Recently, DOX has been loaded on graphene oxide and other nanocomposites.[29−33] Regular Raman microscopy, as well as surface enhanced Raman spectroscopy (SERS) were used to detect DOX in various cell lines and real samples.[34−39] Here, optical signaling of the presence of DOX (deposited from solution) is demonstrated *via* three independent channels: (1) graphene enhanced Raman spectra of analyte (DOX), (2) Raman shift of monolayer graphene (MLG), and (3) photoluminescence (PL) shift of single-layer MoS$_2$ (Figure 1).

Currently, two major approaches are implemented in biosensor technology: label-free and label-based sensing. While the latter shows high selectivity limited only by our ability to find a high-optical-contrast receptor with the best binding to known analyte, the former is much more versatile, especially in terms of sensing a wide range of analytes, enabling agnostic biosensing, and being capable to detect yet unknown biothreats for which the receptors have not been developed. Though very promising, label-free biosensors require additional calibration due to lower specificity. To solve the problem, sensing multiplexing has been applied.[40−42] Multichannel output for such methods often needs to be combined with machine learning in order to convert multidata to readable test results by correlation of different channels and other mathematical methods.[40,42]

In order to achieve multiplexed detection, arrays of different sensors could be integrated in one device.[43] To avoid unnecessary complexity of integration, mutimodal sensing materials and heterostructures are developed.[44−47] Here, we demonstrate potential of vertical heterostructure of monolayer graphene/transition metal dichalcogenide (TMDC) (shown in Figure 1a), for multiplexed detection of doxorubicin by measuring response of 2D materials in three optical channels: graphene enhanced Raman scattering (GERS) of molecular fingerprint modes of the molecule itself (Figure 1b), MoS$_2$ photoluminescence (Figure 1c), and graphene Raman shift (Figure 1e,f).

RESULTS/DISCUSSION

Label-Free Detection of Doxorubicin. Molybdenum disulfide, a typical TMDC 2D material, is known to show a strong PL signal,[48] which can be modulated by the adsorption of molecular species.[49−55] Figure 1c shows a profound change in the PL spectrum of MoS$_2$ photoluminescence (PL) after incubation in a 172 nM solution of DOX for 15 min (the large area integrated PL is presented here; to not be confused with local micro-PL discussed below—note corresponding schematic inset in the top right). In order to understand physical mechanisms resulting in the DOX recognition, the PL band is fitted with individual excitation lines: as shown in the inset of

https://doi.org/10.1021/acsnano.1c09335
ACS Nano XXXX, XXX, XXX−XXX

Table 1. PL Fit Parameters for Figure 1d (with/without DOX)

	trion			A-exciton			B-exciton		
	ω_c, eV	γ, meV	P, cts.	ω_c, eV	γ, meV	P, cts.	ω_c, eV	γ, meV	P, cts.
with DOX	1.739 ± 0.002	60. ± 3.	32 ± 4	1.815 ± 0.0002	82.0 ± 0.3	793 ± 4	1.953 ± 0.001	135.8 ± 2.	203 ± 1
w/o DOX	1.719 ± 0.003	60. ± 9.	15 ± 3	1.806 ± 0.002	90.7 ± 0.3	586 ± 3	1.955 ± 0.002	135.0 ± 2.	197 ± 2

Table 2. Measured GERS Enhancement Factors for Major Fingerprint Raman Lines of DOX

Raman line position, cm^{-1}	1236	1244	1260	1268	1326	1434	1613
GERS enhancement factor	6.4	7.0	23.3	23.3	1.8	2.9	2.1

Figure 1d, the MoS_2 optical transitions include typical B- and A-exciton subbands, trion (X^-), and, often, additional localized modes. Here, the shifts in mode peak position ($\Delta\omega$), peak intensity (ΔP), and width ($\Delta\gamma$) are indicative for analyte absorption, resulting in subsequent charge transfer/doping and strain imposed in the 2D material. These shifts are specific for an analyte and depend on the amount of analyte: panel d and data in Table 1 provide the values for DOX analyte for a given concentration. While upper B-exciton is barely influenced by the drug molecules (a small intensity difference is detected, see the B-arrow in panel d), both A-exciton and trion are red-shifted and have a lower intensity and larger peak width, which all together lead to the spectral differences in panel c. The ability to detect DOX at a low (sub-micromolar) concentration (and differentiate it from other components of a complex solution) would depend on the amount of signal over the noise for the biosensor. Importantly, the variation of the signal in the pristine biosensing material (without analyte) adds to the total uncertainty and reduces the device performance, as we discuss below.

Agnostic detection of a chemical or biothreat requires multiplexing the receptor signal with additional channels, as there is no calibrated negative control (*i.e.*, there is no calibration for desired analyte signal vs off-target components). In order to differentiate the signal from DOX against any other molecule potentially causing PL modulation, we measured the characteristic fingerprint Raman spectrum of DOX. Figure 1b shows the Raman spectrum of the DOX/DMSO solution (cyan curve). However, DOX Raman lines (highlighted by red arrows) are mixed, superimposed, and even obscured with the DMSO (background) response (cyan arrows). Furthermore, the line intensity of analyte would be comparable to the background even at a relatively high DOX concentration. On the contrary, when deposited on a graphene surface, most of the DOX lines[37] became clearly visible, due to a significant GERS enhancement of the Raman signal of DOX (comparing red and cyan curves). Table 2 summarizes the amount of signal enhancement for particular lines. In our sample with only two substances, the intensity of the fingerprint lines of DOX already allows us to confirm the analyte structure and determine the presence of analyte (we note that it cannot be extracted from PL data channel alone, which could respond to other components of sample). While in general, for an agnostic biosensor, the whole Raman spectrum should be analyzed by machine learning correlation analysis of the data.[19,40,42] Here, GERS, the second data channel, complements the PL detection. PL channel provides information on the concentration of the drug (while the intensity of the GERS signal depends on enhancement factors and cannot be used to measure the amount of analyte).

As Figure 1b shows, several DOX lines are superimposed with the Raman spectrum of graphene (gray curve corresponds to MLG reference), specifically with D- and G-lines near 1350 and 1600 cm^{-1}. While obscuring some of the DOX modes, graphene Raman spectra should be analyzed itself, yielding yet another channel, to be multiplexed with the PL and GERS data (note that analyte fingerprint lines should not coincide with graphene modes to be detected, which sets a limitation to sensing with GERS). Parts e and f of Figure 1 show a pronounced red shift and the width increase for two major lines of graphene, G- and 2D-band, upon interaction with the DOX analyte (red). Panels g–l show detailed statistical information on the modulation of both line position and width for both modes; in contrast with previous optical data, each data point in this figure corresponds to a small local region on the sample, less than 0.1 μm^2, diffraction limited (note a corresponding inset schematics in figure, showing a focused light beam). Clearly, the data points aggregate in two separate clusters; though, point-to-point variability due to non-uniformity of the signal is non-negligible for 2D-mode (cf. $\Delta\gamma/\Delta\omega$ correlation plot in panel h and partial distribution functions in panels k and l). Statistical distribution of the data from g–l contains important information about the material/sample, which will be elaborated in detail next.

Stability of 2D van der Waals Heterostructure Materials. Electron microscopy of MoS_2/graphene vertical heterostructure, fabricated as described in the Methods section, reveals structural non-uniformities. A few typical images of three randomly selected single-layer MoS_2 islands, coated with MLG, are shown in Figures 2a,e and 3e. White nanocrystallites, likely made of insulating molybdenum oxide, charged under an e-beam, are seen either in the center of the island (metal nucleation site) or at the edge (metal precipitation site); in some cases, those grow to microcrystals of Mo_2O_3 (see Figure 2e) of characteristic triangular (or rectangular, not shown here) shape and size up to 1/2 μm. Graphene seems to be conformal to the substrate, making short wrinkles between nanoscale posts (10–20 nm tall).

While the surface of MoS_2 islands appears mostly uniform in scanning electron microscopy (SEM) image, optical properties of 2DM demonstrate substantial variation in agreement with larger scatter of Raman and PL distribution (Figures 1 and 3). The variability of PL in pristine material (not determined by SEM morphology characterization) could produce uncertainty in detection of the analyte. In order to find the physical origin for such a variation, scattering scanning near-field optical microscopy (sSNOM) has been applied. Careful alignment of large area scans of the same heterostructure allows us to correlate different characterization channels (including SEM, scanning probe imaging, as well as PL and Raman microscopy, having a lower resolution though). In Figure 2b–d, the

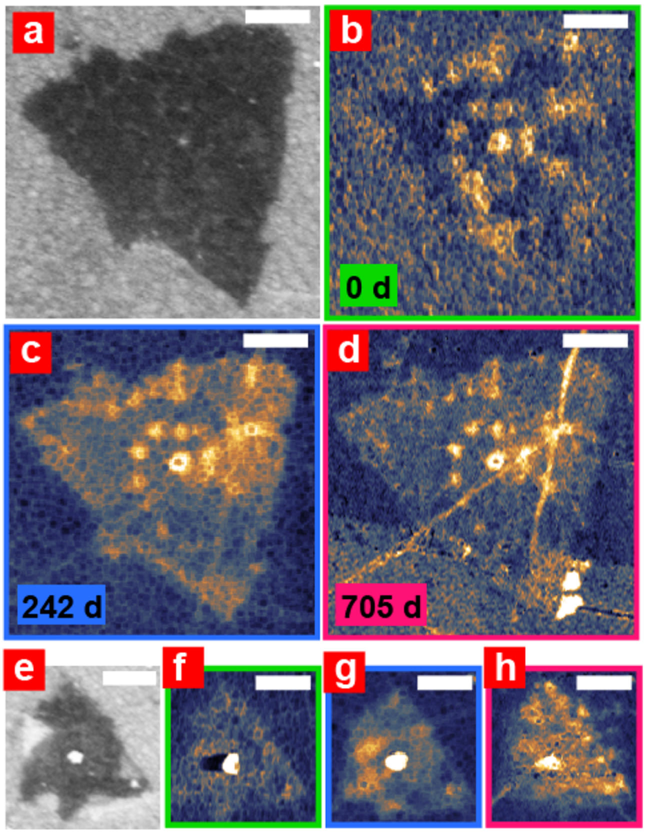

Figure 2. Stability test of MoS_2/graphene vertical heterostructure. Scanning electron microscopy (SEM) (a and e) and scattering scanning nearfield optical microscopy (sSNOM) (b–d and f–h) images of two MoS_2 islands coated with monolayer graphene, randomly selected. The island (a) shows nearly zero degradation after 242 days in ambient—from (b) to (c), neither after 705 days—from (b) to (d); the island (e) was selected near a tear in MLG and shows (g) partial oxidation near the central micro-crystallite of molybdenum after 242 days, followed by (h) almost complete oxidation of MoS_2 surface after 705 days (note: the frame color corresponds to aging, from green to red.) All scale bars are 1 μm.

sSNOM image (second harmonic optical amplitude, see the Methods section for details) reveals variation of the surface impedance of MLG/MoS_2 heterostructure at the submicrometer scale not captured by SEM (or AFM). We argue that a series of bright regions (on the darker background of MoS_2) correspond to the local defects of the TMDC material. Indeed, we regularly observe such a contrast at the edge of the island, which is known to be prone to partial oxidation. Similar regions in the bulk of the island should correspond to concentrated sulfur vacancies, reactive to oxygen, and formation of oxy-sulfate regions, often appearing as nanoscale posts that ruckle graphene around. The series of maps in Figure 2b–d,f–h show the evolution of such regions protected (or non-protected) by graphene coating: the larger island (a), covered with intact MLG, preserves the same number of partially oxidized regions after nearly 2 years in ambient, except for a small oxide crystal grown in the bottom right corner, where a trench in graphene (dark line) opens an access to the air. On the contrary, the small island (e) has the MLG coating cracked; as a result, the surface is slowly oxidized over the course of the retention period, almost entirely on the map in panel h. The sSNOM mapping also shows that the large graphene wrinkles (bright diagonal lines in panel d) do not lead to an alteration of the optical properties with aging. On the opposite, the oxy-sulfate regions, which show sSNOM contrast to the bulk, as shown below, do generate non-uniform doping of the MoS_2 and (graphene), thus leading to the PL variability over the sample.

Local fluctuations of PL in the pristine material were analyzed in another island of the same 2DM vertical heterostructure mapped in Figure 3 by PL in the inset in panel a and by SEM in panel e (to be correlated to high-resolution sSNOM images of the same island in Figures 4b and 5h, by optical amplitude and phase). Several features are clearly resolved: graphene ruptures (not reaching the island), an oxide crystallite at the left edge of the island, a few oxy-sulfate nanoposts and graphene wrinkles around the posts, and several regions of darker SEM contrast (likely, more conductive than bare MLG), potentially indicating doping/Fermi level variation. Confocal PL image of the same area is presented in Figure 3a, inset. The large non-uniformity of PL intensity is followed by a substantial variability of PL line shape (*cf.* the curves in main panel taken at three locations shown in the inset). Similar to the large area PL data in Figure 1c, the main variability of micro-PL results from the A and X^- states, to be

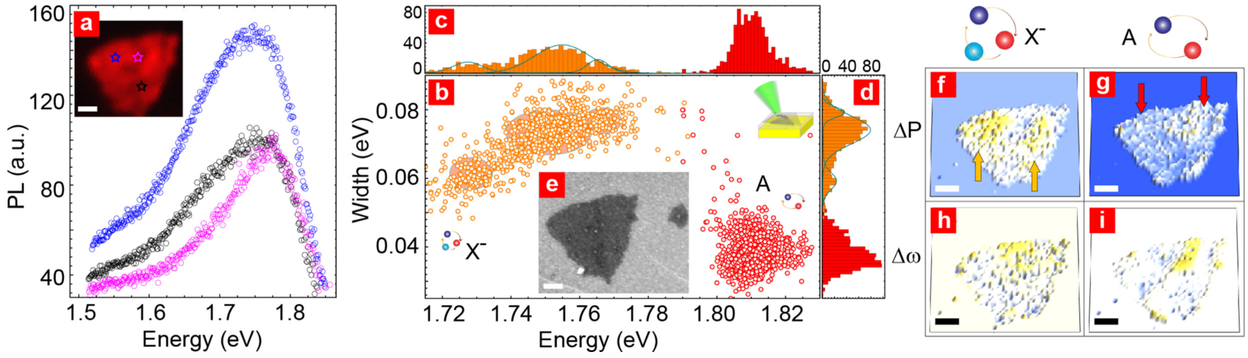

Figure 3. Local PL characterization of MLG/MoS_2 heterostructure. (a) Single-point PL spectra of the MoS_2 island in (e). (inset) Total PL intensity map; stars show locations for the point spectra of the same color in main panel. (b) Correlation plots and (c and d) partial distribution functions for peak position and width for A-exciton (red) and trion (orange) lines, measured locally; several clusters are visible in trion data, highlighted by ovals in correlation plot and Gaussian envelope curves in distributions. (f–i) Confocal maps of MoS_2 PL: (top row) fitted intensity and (bottom row) peak position for (left) trion and (right) A-exciton; arrows show regions of higher PL intensity for trion (lower for A-exciton). All scale bars are 1 μm.

https://doi.org/10.1021/acsnano.1c09335
ACS Nano XXXX, XXX, XXX−XXX

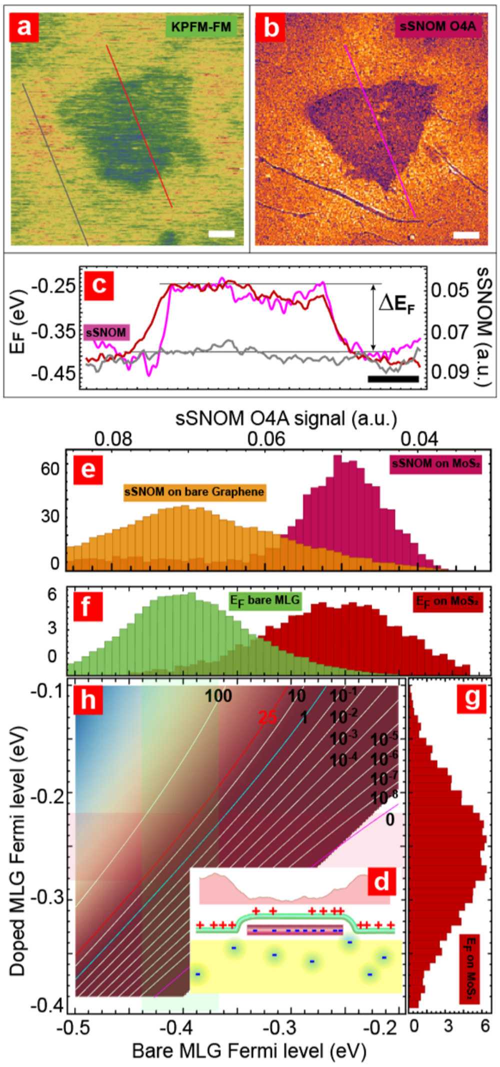

Figure 4. Correlation of MLG work function data with sSNOM optical surface impedance. Aligned maps for (a) KPFM and (b) sSNOM (fourth harmonic) amplitude. (c) Cross section profiles across the MoS_2 area (KPFM, red and sSNOM, pink) vs MLG reference (KPFM, gray), taken along the lines of the same color in (a and b). Inset (d) shows schematics of charge transfer in the vertical heterojunction on the SiO_2 substrate with negative charge traps. Pink curve outlines the variation of MLG work function. (f and g) Partial distribution functions for measured E_F in bare graphene (off island, green) and graphene doped by the MoS_2 (on island, red) from the KPFM map in (a). (e) Partial distribution functions for sSNOM signal from (b) to calibrate near-field signal by E_F. Note common abscissa axis for panels (f and h), not (e). (h) Calculated electron density in MoS_2 heterostructure, log-scale, vs Fermi levels in bare/doped graphene off/on the island. All scale bars are 1 μm.

analyzed separately. Panel b presents the correlation plot for fitted PL peak position and width for A-exciton (red) and trion (orange) states by the local optical probe on the surface of the MLG/MoS_2 heterostructure. MicroPL reveals a large non-uniformity in optical signal. Trion partial distribution functions for both $\Delta\gamma$ and $\Delta\omega$ show three major clusters (highlighted by ovals in panel b and green curves in c and d), which correspond to the regions of heterostructure where materials properties are locally modulated.

Maps in panels f–i show actual distribution of the peak position, $\Delta\omega$, and peak intensity, ΔP, with diffraction limited resolution. Importantly, the intensity maps show the anticorrelation for the PL strength of A-exciton and trion (as indicated by red and orange arrows): the trion PL is the highest where the A-exciton PL is depressed, to be compared with locations for trion-dominated (blue/black) and exciton-dominated (purple) PL curves in panel a. Such a correlation may result from the non-uniform doping of the MoS_2 island. Indeed, in a highly doped area, the neutral excitons are bound to free charges and, thus, converted into trions.[49]

Multidimensional Characterization of Heterostructure Materials. Although it is useful to shed the light on the PL variability, the confocal PL characterization neither has enough spatial resolution nor enables in assessing the MoS_2 doping level to uncover the mechanisms of non-uniform optical signaling. Instead, we developed a multidimensional imaging combining sSNOM and Kelvin probe force microscopy (KPFM) to be correlated with PL (and Raman) microscopy. In Figure 4a,b, two maps of the same island—using a KPFM (work function) channel and sSNOM (optical surface impedance) channel—show identical contrast, as further detailed in panel c where the cross section profiles allow us to quantify the variation of the Fermi level of graphene above the MoS_2 layer. The profile of work function is schematically shown in Figure 4d. Charge transfer in the vertical heterojunction decreases the carrier density in both graphene and MoS_2 underneath, thus decreasing the magnitude of graphene work function and doping level. The KPFM probe is in contact with the outermost layer of the heterostructure, graphene, thus it measures the work function of MLG. Graphene above the island appears negatively doped by MoS_2. The MLG Fermi level, taken with respect to the graphene Dirac point, is negative, corresponding to p-doping.

Statistical distribution of the Fermi level values of graphene on/off the island is shown in panel f by a red/green histogram. Knowing E_F in bare graphene (from other area of the sample) and E_F in the vertical heterostructure allows us to calculate the MoS_2 doping level. Indeed, the leveling of E_F in both materials comprising a heterostructure and conservation of total charge constitute the equations relating all doping levels (Figure 4h). Details of the calculation are presented in the Methods section. Using median values for E_F, in this sample, the MoS_2 doping can be estimated to lie in the range $1{-}25 \times 10^{12}$ cm^{-2}, which is further corroborated by independent Raman data below.

Comparison of the KPFM and sSNOM profiles in Figure 4c, as well as the distribution functions in Figure 4e,f, allows us to calibrate the near-field signal in terms of the Fermi level of the heterostructure. Then, one could interpolate the charge transfer/doping data to the nanometer features, only resolved by sSNOM (such as wrinkles, oxy-sulfate regions, *etc.*) and, thus, determine the origin for PL non-uniformity.

Enhanced resolution of sSNOM allows us to determine five sources of non-uniform doping in the vertical van der Waals heterostructure shown schematically in Figure 4d. (i) The primary doping is defined by conditions of the MoS_2 synthesis: it is known that often the stoichiometry of TMDC is slightly off the equilibrium values. Deficiency in sulfur leads to the creation of surface vacancies,[56] typically resulting in n-doping.[57] (ii) Filling of the S-vacancy with oxygen or CH-group yields weaker n- or p-doping,[49,58] which was shown to be localized near the defect site.[59] (iii) In Mo-abundant synthesis, small microcrystallites of metal molybdenum form,

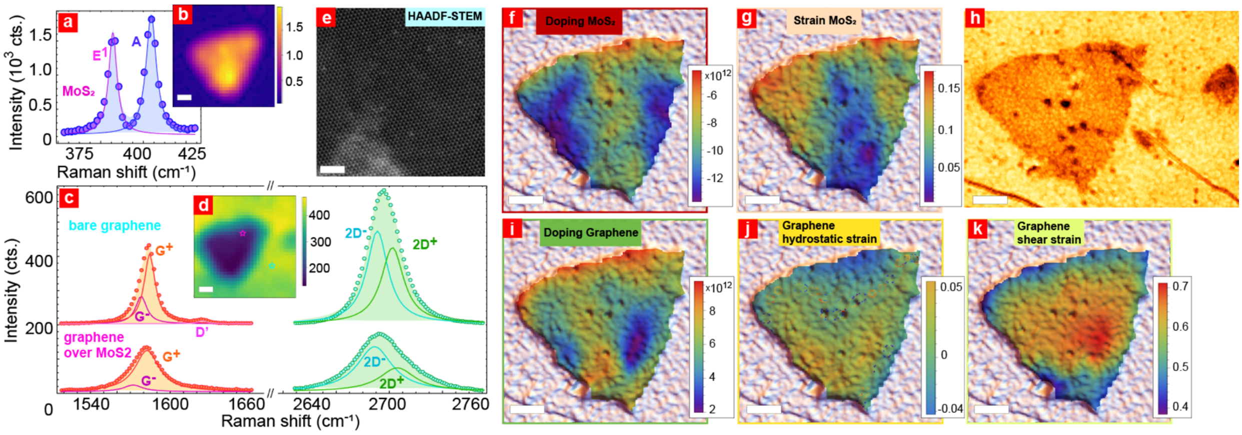

Figure 5. Raman mapping of doping and strain non-uniformity in the heterostructure. (a) Typical MoS_2 Raman spectrum, fitted with E^1 and A-lines. (b) A-line intensity map. (c) Typical Raman spectra for MLG off/on MoS_2 island, fitted by G (orange), D' (pink), and 2D (green) lines; splitting of G- and 2D-lines is shown in the fit. (d) Raman map of 2D-amplitude showing the island location, *cf.* map in (b). (e) High-angle annular dark-field scanning transmission electron microscopy (HAADF-STEM) image of MoS_2 lattice: notice grain boundaries and individual defects; scale bar is 2 nm. (f and g) Calculated doping and strain for MoS_2 layer overlaid with a SEM map; (h) sSNOM phase image of the same area. (i−k) MLG doping, hydrostatic, and shear strain maps. All scale bars, except in (e), are 1 μm.

later oxidized to MoO_x, or forming MoO_xS_y domains. (iv) In the heterostructure, work function and/or Fermi level difference between the layers results in charge transfer between the layers. Typically p-doped MLG would become an acceptor for electrons transferred from n-doped MoS_2. Finally, (v) the Si/SiO_2 substrate, which supports the heterostructure, is known to have a high density of traps at the interface. Such traps, if charged, produce a substantial shift of the Fermi level in all 2DM layers above it, generating a random Coulomb potential for charge carriers both in MoS_2 and graphene.

Additional evidence for the existence of defects/vacancies in TMDC lattice and an estimate for defect density is provided by high-angle annular dark-field (HAADF) scanning transmission electron microscopy (STEM) imaging. Figure 5e shows an atomic resolution map of a typical MoS_2 island. The boundary between dark area and the lower contrast area likely reflects the grain boundary, which separates regions of different lattice orientation. Such a twin boundary produces strain and may result in localization of electronic states. Furthermore, several (3-fold) individual defects are seen in the STEM image (approximately half a dozen per 200 nm^2, which corresponds to *ca.* 3×10^{12} cm^{-2} density).

Multiple sources of optical non-uniformity, stemming from the variation of the doping level, have been further studied with micro-Raman imaging: typical Raman spectra of MLG/MoS_2 heterostructure are shown in Figure 5a,c. Panel a presents A- and E^1-modes of the MoS_2 layer; an A-intensity map is shown in the inset of b. Mode frequencies, fitted as in a, allow us to determine the strain and doping[60] of the island underneath the graphene, generating the maps presented in panels f and g (see the Methods section for details). Consistent with the KPFM data in Figure 4a, MoS_2 doping is lower along the vertical axis of the island; thus, both the amount of charge transfer and graphene E_F should be lower. Charge doping and strain in graphene have been calculated using a similar procedure.[61,62] Upper/lower curves in panel c correspond to MLG Raman lines off/on TMDC, where the location of the island is clearly seen, *e.g.*, in the map of 2D-amplitude in panel d. Parts i and j of Figure 5 show graphene doping and isotropic/hydrostatic strain. Furthermore, the splitting of the G- and 2D-doublet modes (see the fitted curves in panel c) yields[63] the shear (non-isotropic) component of the strain (panel k).

A high-resolution map reveals that the hole carrier density in graphene increases next to the location of a large MoO_x crystallite, which should indicate additional chemical doping. Besides doping, all nanoscale features of heterostructure morphology make contributions to the uniform and non-uniform components of graphene strain, thus making the Raman line width larger than the natural width,[61] due to the statistical broadening.

Multiplexed Biosensing of DOX. Figure 6 demonstrates an example of multiplexed label-free detection of DOX analyte *via* three independent optical channels. For a test sample, a mixed solution was prepared containing DOX, the desired analyte, together with a fumaric acid (FA) in excess *ca.* 3.6× concentration, to mimic the non-specific component of a real

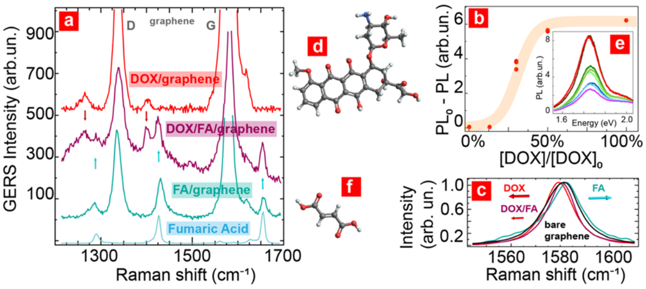

Figure 6. Multiplexed label-free biosensing of DOX analyte. (a) GERS selective detection of DOX vs fumaric acid (FA). The purple curve shows the GERS spectrum of a mixed solution of DOX and FA to be compared with pure DOX GERS (red) and pure FA GERS (cyan). Arrows indicate the coincidence of fingerprint peaks of each analyte (*cf.* Raman spectrum of bare FA, light blue). The largest peaks correspond to D- and G-modes of graphene. (b) Concentration dependence of the MoS_2 integrated PL signal. Maximum concentration of DOX was 172 nM (100%). Inset (e) shows actual PL data. (c) Graphene Raman shift upon analyte adsorption: pure FA demonstrates a blue shift, while pure DOX shows a substantial red shift of the G-peak; a little red shift was found for mixed solution (color code is the same as in panel (a)). Middle insets show (d) DOX and (f) FA molecular structures.

sample. Since the label-free PL signal of MoS_2 should be sensitive to multiple substances, we used a GERS channel to determine the existence of a specific analyte (Figure 6a).

The purple curve corresponds to the GERS spectrum of the mixed solution containing fingerprints of both DOX, the analyte, and FA, the contaminant. Red and cyan curves for pure DOX and pure FA GERS signals are shown for comparison (as well as the Raman spectrum for solid FA, light blue). Since the target and off-target molecules have different structure (as shown in panels d and f, respectively), their fingerprint modes do not overlap and are clearly distinguished (see arrows of the same color).

Figure 6b shows the sensitivity of the MoS_2 PL channel to DOX concentration: a typical sigmoid curve for differential PL signal has a cutoff at *ca.* 60 nM (note that the concentration was normalized to the maximum DOX concentration of 172 nM). The inset in e presents the original spectral data.

Finally, Figure 6c shows the shift of the graphene Raman G-band. For given analyte and off-target molecule, DOX vs FA, the G-band has the opposite shift—red and blue shifts, respectively (see arrows). Note that there is partial compensation of the red shift in the mixed solution (color code is the same as in panel a). Thus, a single Raman channel alone should not be used for biosensing; while as a component of multimodal optical signal, it complements GERS and PL data.

CONCLUSIONS

Cumulatively, the multidimensional characterization data above revealed the existence of non-uniformities in 2D materials at the nanoscale and allowed for the identification of doping and/or strain variations as the origin of statistical distribution of the optical properties. The latter results in the variability in optical signals used in all three recognition channels for multiplexed sensing (PL shift, Raman spectroscopy, and GERS). When integrated over the device area, such a variability in local response would translate in a broadening of the biosensing spectral signal, thus raising device-to-device variability and, ultimately, lowering the sensitivity and the limit-of-detection by increasing background and/or systematic error. While the variability of individual device response often could be addressed by careful calibration against known analytes, such a fluctuation and spread of the integrated response would affect biosensing accuracy and, certainly, reduce the ability to perform precise biosensing in the agnostic detection mode. The presented study suggests that, in order to improve the performance of biosensors based on 2DM heterostructures, non-uniformity of doping and strain—two major mechanisms for optical signal variation—must be addressed. Currently, most of 2DM heterostructures are fabricated by transfer methods, which are known to produce both strain and doping[64−66] (especially for wet transfer). New methods of strain-free and doping-free transfer need to be developed.[64,67] Alternatively, such heterostructure materials should be fabricated *in situ*, in a synthetic facility, to preserve the layer epitaxy and exclude contamination between the layers.

METHODS

Sample Fabrication. The monolayer MoS_2 was grown on a Si substrate with 300 nm thick SiO_2 by a chemical vapor deposition (CVD) method as described in ref 51. Optimization of the synthesis parameters and stoichiometric ratio of molybdenum to sulfur resulted in producing triangular MoS_2 islands with a low defect density (*cf.*, STEM image in Figure 5e), predominantly single layers, with a low surface coverage. Monolayer graphene was grown by CVD on Cu foil. MLG was transferred onto MoS_2 using the conventional PMMA assisted transfer technique.[68] The SEM images of resulted heterostructures are shown in Figures 2a,e and 3e. DOX and FA samples were prepared by diluting original solution (obtained by dissolving doxorubicin hydrochloride (DOX) and fumaric acid disodium salt (FA) in dimethyl sulfoxide (DMSO) (from Sigma-Aldrich) at *ca.* 172 and 625 nM concentrations, respectively) and applying it to the MoS_2/Si and/or MLG/MoS_2/Si substrates for characterization.

Sample Characterization. SEM sample imaging was performed on a field emission scanning electron microscope Zeiss Auriga FIB/FESEM. Atomic resolution images of monolayer MoS_2 samples transferred onto Quantaifoil TEM grids were recorded using Nion Ultra HAADF-STEM operating at 60 kV with third-generation C3/C5 aberration corrector and a 0.5 nA current in an atomic-size probe ∼1.0−1.1 Å (NCATSU). Confocal PL and Raman characterization were performed using a Horiba Jobin Yvon LabRAM HR-Evolution Raman system; 488 nm (for Raman) and 532 nm (for PL) laser excitation wavelengths were used. A Horiba XploRA Raman system was used for taking the Raman spectra at 532 nm of excitation. The analysis of PL and Raman characterization was performed using home-written codes.

sSNOM maps were collected using a scattering type scanning near-field optical microscope (custom-built Neaspec system) in pseudo-heterodyne mode (tapping amplitude ∼70 nm, ARROW-NCPt probes by Nanoworld <25 nm radius), excitation by a CW quantum cascade laser (MIRCat by Daylight) at power <2 mW in focal aperture at 1577−1579 cm^{-1} (6.333−6.341 μm). The amplitude and phase of high order harmonics (≥2) are proportional to the local impedance of the sample under the tip.

The AFM/KPFM was performed using Dimension Icon AFM in PeakForce Kelvin probe force microscopy in frequency modulated mode (PFKPFM-FM, Bruker Nano Inc., Santa Barbara, CA) utilizing a PFQNE-AL probe (Bruker SPM Probes, Camarillo, CA). Prior to measuring the samples, the KPFM response of the probe was checked against an Au−Si−Al standard and the work function of the Al reference metal layer was calibrated against a freshly cleaved highly oriented pyrolytic graphite (HOPG) reference sample (PFKPFM-SMPL, HOPG-12M, Bruker SPM Probes, Camarillo, CA); 4.6 eV was used for the work function reference value for HOPG.

Modeling of Charge Transfer. Charge exchange between MoS_2 and graphene in the vertical heterostructure is governed by a set of equations that include the following: relation of charge density to the density of states and the Fermi level, Fermi level continuity (including proper work function difference), electrostatic potential from the substrate impurities, and interlayer capacitance (see the Supporting Information). As a result, the doping level of either component of the heterostructure can be determined from any two independent Fermi level parameters (graphene or TMDC, before or after contact). In this work, we used experimentally measured values of graphene Fermi level before and after contact with TMDC. Since there is a range of measured values for E_F and $E_F^{(o)}$, the doping level of MoS_2 should also vary, as shown by semitransparent boxes in the density plot in Figure 4h.

ASSOCIATED CONTENT

Supporting Information

The Supporting Information is available free of charge at https://pubs.acs.org/doi/10.1021/acsnano.1c09335.

Discussions of strain and doping analysis, characterization by peak-force Kevin probe force microscopy, calculation of charge density in MLG and in MoS_2 monolayer, and PL and GERS data, table of measured Raman lines of FA and DOX, and figures of additional Raman data, maps showing the fitted parameters for splitting of 2D peaks, G peaks, and MoS_2 peaks, AFM topography and KPFM signal, calculated work function distribution, band structure of MoS_2/graphene van der Waals heterojunction, and MoS_2 PL spectra (PDF)

Animation file representing some of the channels of multidimensional characterization of a particular van der Waals vertical heterostructure (MP4)

AUTHOR INFORMATION

Corresponding Authors

Tetyana Ignatova − *Department of Nanoscience, University of North Carolina at Greensboro, Greensboro, North Carolina 27401, United States;* orcid.org/0000-0003-3859-6367; Email: t_ignato@uncg.edu

Slava V. Rotkin − *Department of Engineering Science and Mechanics, The Pennsylvania State University, University Park, Pennsylvania 16802, United States; Materials Research Institute, The Pennsylvania State University, University Park, Pennsylvania 16802, United States;* orcid.org/0000-0001-7221-1091; Email: rotkin@psu.edu

Authors

Sajedeh Pourianejad − *Department of Nanoscience, University of North Carolina at Greensboro, Greensboro, North Carolina 27401, United States*

Xinyi Li − *Department of Engineering Science and Mechanics, The Pennsylvania State University, University Park, Pennsylvania 16802, United States*

Kirby Schmidt − *Department of Nanoscience, University of North Carolina at Greensboro, Greensboro, North Carolina 27401, United States*

Frederick Aryeetey − *Department of Nanoengineering, North Carolina A&T State University, Greensboro, North Carolina 27401, United States*

Shyam Aravamudhan − *Department of Nanoengineering, North Carolina A&T State University, Greensboro, North Carolina 27401, United States*

Complete contact information is available at: https://pubs.acs.org/10.1021/acsnano.1c09335

Author Contributions

$^{\perp}$T.I. and S.V.R. are presenting authors.

Notes

This manuscript was previously uploaded to a preprint server.[69]

The authors declare no competing financial interest.

ACKNOWLEDGMENTS

Authors are personally thankful to Drs. T. Tighe, T. Williams, and M. Wetherington (MCL, PSU). S.V.R. acknowledges NSF support (CHE-2032582). T.I. and K.S. acknowledge NSF support (CHE-2032601). T.I. acknowledges a Sample Grant from The Pennsylvania State University 2DCC-MIP, which is supported by NSF cooperative agreement (DMR-1539916). Work at PSU sSNOM facility has been partially supported by NSF MRSEC (DMR-2011839). Part of this work was performed at the Joint School of Nanoscience and Nanoengineering (JSNN), a member of the Southeastern Nanotechnology Infrastructure Corridor (SENIC), and National Nanotechnology Coordinated Infrastructure (NNCI), which is supported by the NSF grant (ECCS-1542174). Scanning transmission electron microscope imaging was conducted at the Center for Nanophase Materials Sciences at ONRL, which is a DOE Office of Science User Facility.

REFERENCES

(1) Kostarelos, K.; Novoselov, K. S. Graphene Devices for Life. *Nat. Nanotechnol.* **2014**, *9*, 744−745.

(2) Bolotsky, A.; Butler, D.; Dong, C.; Gerace, K.; Glavin, N. R.; Muratore, C.; Robinson, J. A.; Ebrahimi, A. Two-Dimensional Materials in Biosensing and Healthcare: From In Vitro Diagnostics to Optogenetics and Beyond. *ACS Nano* **2019**, *13*, 9781−9810.

(3) Zhu, X.; Ding, R.; Wang, Z.; Wang, Y.; Guo, X.; Song, Z.; Wang, Z.; Dong, M. Recent Advances in Synthesis and Biosensors of Two-Dimensional MoS_2. *Nanotechnology* **2019**, *30*, 502004.

(4) Daus, A.; Vaziri, S.; Chen, V.; Koroglu, C.; Grady, R. W.; Bailey, C. S.; Lee, H. R.; Schauble, K.; Brenner, K.; Pop, E. High-Performance Flexible Nanoscale Transistors Based on Transition Metal Dichalcogenides. *Nature Electronics* **2021**, *4*, 495.

(5) Lee, J.; Dak, P.; Lee, Y.; Park, H.; Choi, W.; Alam, M. A.; Kim, S. Two-Dimensional Layered MoS_2 Biosensors Enable Highly Sensitive Detection of Biomolecules. *Sci. Rep.* **2015**, *4*, 7352.

(6) Ayodele, O. O.; Adesina, A. O.; Pourianejad, S.; Averitt, J.; Ignatova, T. Recent Advances in Nanomaterial-Based Aptasensors in Medical Diagnosis and Therapy. *Nanomaterials* **2021**, *11*, 932.

(7) Campuzano, S.; Pedrero, M.; Nikoleli, G.-P.; Pingarron, J.M.; Nikolelis, D.P. Hybrid 2D-Nanomaterials-Based Electrochemical Immunosensing Strategies for Clinical Biomarkers Determination. *Biosens. Bioelectron.* **2017**, *89*, 269−279.

(8) Oh, S.-H.; Altug, H.; Jin, X.; Low, T.; Koester, S. J.; Ivanov, A. P.; Edel, J. B.; Avouris, P.; Strano, M. S. Nanophotonic Biosensors Harnessing van der Waals Materials. *Nat. Commun.* **2021**, *12*, 3824.

(9) Pang, Y.; Yang, Z.; Yang, Y.; Ren, T.-L. Wearable Electronics Based on 2D Materials for Human Physiological Information Detection. *Small* **2020**, *16*, 1901124.

(10) Yen, C.-W.; de Puig, H.; Tam, J. O.; Gomez-Marquez, J.; Bosch, I.; Hamad-Schifferli, K.; Gehrke, L. Multicolored Silver Nanoparticles for Multiplexed Disease Diagnostics: Distinguishing Dengue, Yellow Fever, and Ebola Viruses. *Lab Chip* **2015**, *15*, 1638−1641.

(11) Wang, S.; Li, X.; Chen, Y.; Cai, X.; Yao, H.; Gao, W.; Zheng, Y.; An, X.; Shi, J.; Chen, H. A Facile One-Pot Synthesis of a Two-Dimensional MoS_2/Bi_2S_3 Composite Theranostic Nanosystem for Multi-Modality Tumor Imaging and Therapy. *Adv. Mater.* **2015**, *27*, 2775−2782.

(12) Lee, H.; Choi, T. K.; Lee, Y. B.; Cho, H. R.; Ghaffari, R.; Wang, L.; Choi, H. J.; Chung, T. D.; Lu, N.; Hyeon, T.; Choi, S. H.; Kim, D.-H. A Graphene-Based Electrochemical Device with Thermoresponsive Microneedles for Diabetes Monitoring and Therapy. *Nat. Nanotechnol.* **2016**, *11*, 566−572.

(13) Lei, Y.; Zhao, W.; Zhang, Y.; Jiang, Q.; He, J.-H.; Baeumner, A. J.; Wolfbeis, O. S.; Wang, Z. L.; Salama, K. N.; Alshareef, H. N. A MXene-Based Wearable Biosensor System for High-Performance In Vitro Perspiration Analysis. *Small* **2019**, *15*, 1901190.

(14) Zhang, B.; Pinsky, B. A.; Ananta, J. S.; Zhao, S.; Arulkumar, S.; Wan, H.; Sahoo, M. K.; Abeynayake, J.; Waggoner, J. J.; Hopes, C.; Tang, M.; Dai, H. Diagnosis of Zika Virus Infection on a Nanotechnology Platform. *Nature Medicine* **2017**, *23*, 548−550.

(15) Zhang, Y.; Zheng, B.; Zhu, C.; Zhang, X.; Tan, C.; Li, H.; Chen, B.; Yang, J.; Chen, J.; Huang, Y.; Wang, L.; Zhang, H. Single-Layer Transition Metal Dichalcogenide Nanosheet-Based Nanosensors for Rapid, Sensitive, and Multiplexed Detection of DNA. *Adv. Mater.* **2015**, *27*, 935−939.

(16) Wang, Y.; Tang, L.; Li, Z.; Lin, Y.; Li, J. In Situ Simultaneous Monitoring of ATP and GTP Using a Graphene Oxide Nanosheet-Based Sensing Platform in Living Cells. *Nat. Protoc.* **2014**, *9*, 1944−1955.

(17) Arjmandi-Tash, H.; Belyaeva, L. A.; Schneider, G. F. Single Molecule Detection with Graphene and Other Two-Dimensional Materials: Nanopores and Beyond. *Chem. Soc. Rev.* **2016**, *45*, 476−493.

(18) Sekhon, S. S.; Kaur, P.; Kim, Y.-H.; Sekhon, S. S. 2D graphene oxide-aptamer conjugate materials for cancer diagnosis. *npj 2D Materials and Applications* **2021**, *5*, 21.

(19) Kolesnichenko, P. V.; Zhang, Q.; Zheng, C.; Fuhrer, M. S.; Davis, J. A. Multidimensional Analysis of Excitonic Spectra of Monolayers of Tungsten Disulphide: Toward Computer-Aided Identification of Structural and Environmental Perturbations of 2D Materials. *Machine Learning: Science and Technology* **2021**, *2*, 025021.

(20) Norouzi, M.; Yathindranath, V.; Thliveris, J. A.; Kopec, B. M.; Siahaan, T. J.; Miller, D. W. Doxorubicin-Loaded Iron Oxide Nanoparticles for Glioblastoma Therapy: a Combinational Approach for Enhanced Delivery of Nanoparticles. *Sci. Rep.* **2020**, *10*, 11292.

(21) Chen, J.; Qian, C.; Ren, P.; Yu, H.; Kong, X.; Huang, C.; Luo, H.; Chen, G. Light-Responsive Micelles Loaded With Doxorubicin for Osteosarcoma Suppression. *Frontiers in Pharmacology* **2021**, *12*, 1378.

(22) Zhong, Y.; Meng, F.; Deng, C.; Mao, X.; Zhong, Z. Targeted Inhibition of Human Hematological Cancers in Vivo by Doxorubicin Encapsulated in Smart Lipoic Acid-Crosslinked Hyaluronic Acid Nanoparticles. *Drug delivery* **2017**, *24*, 1482−1490.

(23) He, Y.; Qiu, X. Chidamide Combined with Doxorubicin Leads to Synergistic Anti-Cancer Effect and Induces Autophagy Through Inhibiting the PI3K/Akt/mTOR Pathway in Anaplastic Thyroid Carcinoma. http://biorxiv.org/content/early/2020/05/22/2020.05.19.105288.abstract (accessed 2020-05-22).

(24) Yuan, Z.; et al. Pegylated Liposomal Doxorubicin in Patients with Epithelial Ovarian Cancer. *J. Ovarian Res.* **2021**, *14*, 12.

(25) Carvalho, F. S.; Burgeiro, A.; Garcia, R.; Moreno, A. J.; Carvalho, R. A.; Oliveira, P. J. Doxorubicin-Induced Cardiotoxicity: From Bioenergetic Failure and Cell Death to Cardiomyopathy. *Medicinal Research Reviews* **2014**, *34*, 106−135.

(26) Hofman, J.; Skarka, A.; Havrankova, J.; Wsol, V. Pharmacokinetic Interactions of Breast Cancer Chemotherapeutics with Human Doxorubicin Reductases. *Biochem. Pharmacol.* **2015**, *96*, 168−178.

(27) Mitry, M. A.; Edwards, J. G. Doxorubicin Induced Heart Failure: Phenotype and Molecular Mechanisms. *IJC Heart & Vasculature* **2016**, *10*, 17−24.

(28) Umsumarng, S.; Pitchakarn, P.; Sastraruji, K.; Yodkeeree, S.; Ung, A. T.; Pyne, S. G.; Limtrakul, P. Reversal of Human Multi-Drug Resistance Leukaemic Cells by Stemofoline Derivatives via Inhibition of P-Glycoprotein Function. *Basic & Clinical Pharmacology & Toxicology* **2015**, *116*, 390−397.

(29) Sun, X.; Liu, Z.; Welsher, K.; Robinson, J. T.; Goodwin, A.; Zaric, S.; Dai, H. Nano-graphene oxide for cellular imaging and drug delivery. *Nano Research* **2008**, *1*, 203−212.

(30) Chekin, F.; Myshin, V.; Ye, R.; Melinte, S.; Singh, S. K.; Kurungot, S.; Boukherroub, R.; Szunerits, S. Graphene-Modified Electrodes for Sensing Doxorubicin Hydrochloride in Human Plasma. *Anal. Bioanal. Chem.* **2019**, *411*, 1509−1516.

(31) Hasanzadeh, M.; Hashemzadeh, N.; Shadjou, N.; Eivazi-Ziaei, J.; Khoubnasabjafari, M.; Jouyban, A. Sensing of Doxorubicin Hydrochloride Using Graphene Quantum Dot Modified Glassy Carbon Electrode. *J. Mol. Liq.* **2016**, *221*, 354−357.

(32) Yang, Z.; Yang, D.; Zeng, K.; Li, D.; Qin, L.; Cai, Y.; Jin, J. Simultaneous Delivery of antimiR-21 and Doxorubicin by Graphene Oxide for Reducing Toxicity in Cancer Therapy. *ACS Omega* **2020**, *5*, 14437−14443.

(33) Pei, X.; Zhu, Z.; Gan, Z.; Chen, J.; Zhang, X.; Cheng, X.; Wan, Q.; Wang, J. PEGylated Nano-Graphene Oxide as a Nanocarrier for Delivering Mixed Anticancer Drugs to Improve Anticancer Activity. *Sci. Rep.* **2020**, *10*, 2717.

(34) Zong, C.; Xu, M.; Xu, L.-J.; Wei, T.; Ma, X.; Zheng, X.-S.; Hu, R.; Ren, B. Surface-Enhanced Raman Spectroscopy for Bioanalysis: Reliability and Challenges. *Chem. Rev.* **2018**, *118*, 4946−4980.

(35) Gautier, J.; Munnier, E.; Douziech-Eyrolles, L.; Paillard, A.; Dubois, P.; Chourpa, I. SERS Spectroscopic Approach to Study Doxorubicin Complexes with Fe^{2+} Ions and Drug Release from SPION-Based Nanocarriers. *Analyst* **2013**, *138*, 7354−7361.

(36) Huang, J.; Zong, C.; Shen, H.; Cao, Y.; Ren, B.; Zhang, Z. Tracking the Intracellular Drug Release from Graphene Oxide Using Surface-Enhanced Raman Spectroscopy. *Nanoscale* **2013**, *5*, 10591−8.

(37) Farhane, Z.; Bonnier, F.; Casey, A.; Byrne, H. J. Raman Micro Spectroscopy for in Vitro Drug Screening: Subcellular Localisation and Interactions of Doxorubicin. *Analyst* **2015**, *140*, 4212−23.

(38) Farhane, Z.; Bonnier, F.; Byrne, H. J. Monitoring Doxorubicin Cellular Uptake and Trafficking Using in Vitro Raman Microspectroscopy: Short and Long Time Exposure Effects on Lung Cancer Cell Lines. *Anal. Bioanal. Chem.* **2017**, *409*, 1333−1346.

(39) Litti, L.; Amendola, V.; Toffoli, G.; Meneghetti, M. Detection of Low-Quantity Anticancer Drugs by Surface-Enhanced Raman Scattering. *Anal. Bioanal. Chem.* **2016**, *408*, 2123−2131.

(40) Zhang, K.; Wang, J.; Liu, T.; Luo, Y.; Loh, X. J.; Chen, X. Machine Learning-Reinforced Noninvasive Biosensors for Healthcare. *Adv. Healthcare Mater.* **2021**, *10*, 2100734.

(41) Misun, P. M.; Rothe, J.; Schmid, Y. R. F.; Hierlemann, A.; Frey, O. Multi-Analyte Biosensor Interface for Real-Time Monitoring of 3D Microtissue Spheroids in Hanging-Drop Networks. *Microsystems & Nanoengineering* **2016**, *2*, 16022.

(42) Cui, F.; Yue, Y.; Zhang, Y.; Zhang, Z.; Zhou, H. S. Advancing Biosensors with Machine Learning. *ACS Sens* **2020**, *5*, 3346−3364.

(43) Kalmykov, A.; Huang, C.; Bliley, J.; Shiwarski, D.; Tashman, J.; Abdullah, A.; Rastogi, S. K.; Shukla, S.; Mataev, E.; Feinberg, A. W.; Hsia, K. J.; Cohen-Karni, T. Organ-on-e-chip: Three-Dimensional Self-Rolled Biosensor Array for Electrical Interrogations of Human Electrogenic Spheroids. *Sci. Adv.* **2019**, *5*, No. eaax0729.

(44) Novoselov, K. S.; Mishchenko, A.; Carvalho, A.; Castro Neto, A. H. 2D Materials and van der Waals Heterostructures. *Science* **2016**, *353*, aac9439.

(45) Jeong, S.; et al. Fluorescence-Raman Dual Modal Endoscopic System for Multiplexed Molecular Diagnostics. *Sci. Rep.* **2015**, *5*, 9455.

(46) Ma, Q.; Ren, G.; Mitchell, A.; Ou, J. Z. Recent Advances on Hybrid Integration of 2D Materials on Integrated Optics Platforms. *Nanophotonics* **2020**, *9*, 2191−2214.

(47) AlaguVibisha, G.; Nayak, J. K.; Maheswari, P.; Priyadharsini, N.; Nisha, A.; Jaroszewicz, Z.; Rajesh, K. B.; Jha, R. Sensitivity Enhancement of Surface Plasmon Resonance Sensor Using Hybrid Configuration of 2D Materials over Bimetallic Layer of Cu-Ni. *Opt. Commun.* **2020**, *463*, 125337.

(48) Mak, K. F.; He, K.; Lee, C.; Lee, G. H.; Hone, J.; Heinz, T. F.; Shan, J. Tightly Bound Trions in Monolayer MoS_2. *Nat. Mater.* **2013**, *12*, 207−211.

(49) Mouri, S.; Miyauchi, Y.; Matsuda, K. Tunable Photoluminescence of Monolayer MoS_2 via Chemical Doping. *Nano Lett.* **2013**, *13*, 5944−5948.

(50) Catalan-Gomez, S.; Briones, M.; Cortijo-Campos, S.; Garcia-Mendiola, T.; de Andres, A.; Garg, S.; Kung, P.; Lorenzo, E.; Pau, J. L.; Redondo-Cubero, A. Breast Cancer Biomarker Detection Through the Photoluminescence of Epitaxial Monolayer MoS_2 Flakes. *Sci. Rep.* **2020**, *10*, 16039.

(51) Aryeetey, F.; Pourianejad, S.; Ayanbajo, O.; Nowlin, K.; Ignatova, T.; Aravamudhan, S. Bandgap Recovery of Monolayer MoS_2 Using Defect Engineering and Chemical Doping. *RSC Adv.* **2021**, *11*, 20893−20898.

(52) Barja, S.; et al. Identifying Substitutional Oxygen as a Prolific Point Defect in Monolayer Transition Metal Dichalcogenides. *Nat. Commun.* **2019**, *10*, 3382.

(53) Mitterreiter, E.; et al. The Role of Chalcogen Vacancies for Atomic Defect Emission in MoS_2. *Nat. Commun.* **2021**, *12*, 3822.

(54) Schuler, B.; Cochrane, K. A.; Kastl, C.; Barnard, E. S.; Wong, E.; Borys, N. J.; Schwartzberg, A. M.; Ogletree, D. F.; de Abajo, F. J. G.; Weber-Bargioni, A. Electrically Driven Photon Emission from Individual Atomic Defects in Monolayer WS2. *Sci. Adv.* **2020**, *6*, No. eabb5988.

(55) Thiruraman, J. P.; Fujisawa, K.; Danda, G.; Das, P. M.; Zhang, T.; Bolotsky, A.; Perea-Lopez, N.; Nicolai, A.; Senet, P.; Terrones, M.; Drndic, M. Angstrom-Size Defect Creation and Ionic Transport

through Pores in Single-Layer MoS_2. *Nano Lett.* **2018**, *18*, 1651−1659.

(56) Aryeetey, F.; Ignatova, T.; Aravamudhan, S. Quantification of Defects Engineered in Single Layer MoS_2. *RSC Adv.* **2020**, *10*, 22996−23001.

(57) Komsa, H.-P.; Krasheninnikov, A. V. Native Defects in Bulk and Monolayer MoS_2 from First Principles. *Phys. Rev. B* **2015**, *91*, 125304.

(58) Zheng, X.; et al. Spatial Defects Nanoengineering for Bipolar Conductivity in MoS_2. *Nat. Commun.* **2020**, *11*, 3463.

(59) Nan, H.; Wang, Z.; Wang, W.; Liang, Z.; Lu, Y.; Chen, Q.; He, D.; Tan, P.; Miao, F.; Wang, X.; Wang, J.; Ni, Z. Strong Photoluminescence Enhancement of MoS2 through Defect Engineering and Oxygen Bonding. *ACS Nano* **2014**, *8*, 5738−5745.

(60) Rao, R.; Islam, A. E.; Singh, S.; Berry, R.; Kawakami, R. K.; Maruyama, B.; Katoch, J. Spectroscopic Evaluation of Charge-Transfer Doping and Strain in Graphene/MoS_2 heterostructures. *Phys. Rev. B* **2019**, *99*, 195401.

(61) Neumann, C.; Reichardt, S.; Venezuela, P.; Droegeler, M.; Banszerus, L.; Schmitz, M.; Watanabe, K.; Taniguchi, T.; Mauri, F.; Beschoten, B.; Rotkin, S. V.; Stampfer, C. Raman Spectroscopy as Probe of Nanometre-Scale Strain Variations in Graphene. *Nat. Commun.* **2015**, *6*, 8429.

(62) Mueller, N. S.; et al. Evaluating Arbitrary Strain Configurations and Doping in Graphene with Raman Spectroscopy. *2D Materials* **2018**, *5*, 015016.

(63) Narula, R.; Bonini, N.; Marzari, N.; Reich, S. Dominant Phonon Wave Vectors and Strain-Induced Splitting of the 2*D* Raman Mode of Graphene. *Phys. Rev. B* **2012**, *85*, 115451.

(64) Leong, W. S.; Wang, H.; Yeo, J.; Martin-Martinez, F. J.; Zubair, A.; Shen, P.-C.; Mao, Y.; Palacios, T.; Buehler, M. J.; Hong, J.-Y.; Kong, J. Paraffin-Enabled Graphene Transfer. *Nat. Commun.* **2019**, *10*, 867.

(65) Bousige, C.; Balima, F.; Machon, D.; Pinheiro, G. S.; Torres-Dias, A.; Nicolle, J.; Kalita, D.; Bendiab, N.; Marty, L.; Bouchiat, V.; Montagnac, G.; Souza Filho, A. G.; Poncharal, P.; San-Miguel, A. Biaxial Strain Transfer in Supported Graphene. *Nano Lett.* **2017**, *17*, 21−27.

(66) Banszerus, L.; Janssen, H.; Otto, M.; Epping, A.; Taniguchi, T.; Watanabe, K.; Beschoten, B.; Neumaier, D.; Stampfer, C. Identifying Suitable Substrates for High-Quality Graphene-Based Heterostructures. *2D Materials* **2017**, *4*, 025030.

(67) Seo, Y.-M.; Jang, W.; Gu, T.; Seok, H.-J.; Han, S.; Choi, B. L.; Kim, H.-K.; Chae, H.; Kang, J.; Whang, D. Defect-Free Mechanical Graphene Transfer Using n-Doping Adhesive Gel Buffer. *ACS Nano* **2021**, *15*, 11276.

(68) Gao, L.; Ren, W.; Xu, H.; Jin, L.; Wang, Z.; Ma, T.; Ma, L.-P.; Zhang, Z.; Fu, Q.; Peng, L.-M.; Bao, X.; Cheng, H.-M. Repeated Growth and Bubbling Transfer of Graphene with Millimetre-Size Single-Crystal Grains Using Platinum. *Nat. Commun.* **2012**, *3*, 699.

(69) Ignatova, T.; Pourianejad, S.; Li, X.; Schmidt, K.; Aryeetey, F.; Aravamudhan, S.; Rotkin, S. V. Multidimensional Imaging Reveals Mechanisms Controlling Label-Free Biosensing in Vertical 2DM-Heterostructures. https://arxiv.org/abs/2111.09776 (accessed 2021-12-30).